Applied Acoustics 173 (2021) 107656

Contents lists available at ScienceDirect

Applied Acoustics

journal homepage: www.elsevier.com/locate/apacoust

A parametric study of the acoustic properties of thermal cladding systems

C. Churchill [a,*], T. Bednar [a], H. Müllner [b], M. Neusser [c], S. Hinterseer [a]

[a] TU Wien, Austria
[b] TGM, Austria
[c] ACOM Research, Austria

ARTICLE INFO

Article history:
Received 10 July 2020
Received in revised form 1 September 2020
Accepted 2 September 2020
Available online 10 October 2020

Keywords:
Sound insulation
Thermal insulation
Coupling loss factor
Cladding
ETICS
Lightweight

ABSTRACT

Thermal cladding systems have developed and modernised since the first systems were implemented, and predictions of single figure sound insulation improvement, ΔR_W, based on the natural frequency, f_0, of the spring-mass covering may no longer be reliable. To identify aspects of the compound acoustic behaviour due to multiple power flow paths of the thermal insulating system, a statistical energy analysis (SEA) based prediction model was developed. A simplified calculation of sound insulation improvement, ΔR, is described, allowing the high frequency ($f > f_0$) behaviour of thermal cladding systems to be predicted. A parametric study in which the impact of different construction materials in the model is discussed; the damping constants, elastic properties of the interlayer and fixings, number of fixings, thickness and material properties (including bending stiffness) of the weatherproof outer layer and the heavyweight wall are assessed. While agreement within 4.0 dB (mean absolute differences) between calculated and measured results for thick render ($\geq$8.0 mm) and curtain wall systems can be obtained at high frequencies ($f > f_0$) using the simplified methodology, this approach was not successful at predicting single figure values. This is because single figure values are weighted towards the low frequencies. Correlation of calculated f_0 with measured ΔR_W is slightly improved (r.m.s. differences of 2.62 compared with 3.21 using the f_0 calculation methodology in EN ISO12354 Annex D) when a modified method to calculate the combined stiffness is used. To improve predictions further, a methodology must be developed to obtain the transfer function, Y_{tr}, used to calculate non-resonant coupling loss factor due to the spring-mass resonance of thermal cladding on the heavyweight wall. The mobility of the connections, Y_c, should also be accurately characterised to ensure accurate predictions at high frequencies.

1. Introduction

Thermal cladding systems are widely used in construction and consist of; (a) a typical heavyweight wall, (b) a lightweight layer of thermal insulation and (c) a weatherproof cladding system. This generalised description includes ETICS (external thermal insulation composite systems) and curtain wall systems. Over the years thermal cladding systems have developed into the modern systems used today. Key aspects have changed, such as increased thickness of thermal insulation, as thermal insulation requirements have increased, and the refurbishment of old buildings has meant that cladding systems have been added to previously built exterior walls [1–4]. EN ISO 12354-1 (Annex D) [5] provides a simple method to determine the single figure sound insulation improvement, ΔR_W, due to different thermal cladding systems on the basis of the natural frequency, f_0, of the thermal cladding system. This relies on the assumption that the thermal insulation system can be modelled as a simple spring- mass system. EN ISO 10140-1 (Annex G) [6] provides a methodology for measurement. The relationship between the natural frequency and the measured weighted sound insulation improvement of thirty-eight ETICS (e.g. with different dynamic stiffness, render thicknesses and numbers of structural connections), and two curtain walls (e.g. with different cladding systems) is presented in Fig. 1 and compared with the calculation procedure. The spread of the measured results is wide and suggests that the concept of a simple relationship between f_0 and ΔR_W is no longer reliable for modern systems and may no longer be adequate to predict the weighted sound insulation improvement.

A prediction model to capture this more complicated behaviour with an improved understanding of the sound insulation improve-

* Corresponding author.
E-mail address: claire.churchill@tuwien.ac.at (C. Churchill).

https://doi.org/10.1016/j.apacoust.2020.107656
0003-682X/

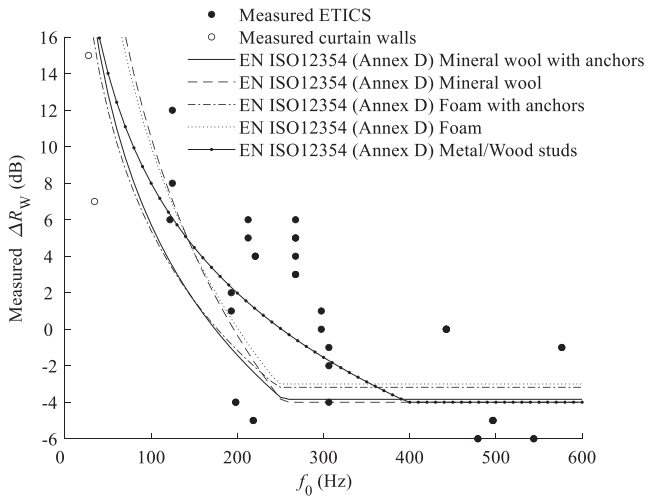

Fig. 1. Plot of ΔR_W due to different ETICS against f_0 of the system, (note that f_0 is estimated using the dynamic stiffness of the interlayer only and does not include the structural fixings). Calculations according to EN ISO 12354 (Annex D) are also depicted.

ment of modern thermal cladding systems across the building acoustics frequency range (50–5000 Hz) is sought. The spring-mass system is usually installed in combination with structural fixings. These may be point connections, line connections or a more complicated framework onto which the weatherproof cladding system may be mounted. The effect of the structural fixings is likely twofold. Firstly, the connections may modify the dynamic stiffness of the elastic interlayer, in the simplest case acting as a spring combination in parallel to increase the stiffness and shift the value of f_0 towards higher frequencies. In this case, the energy transfer is modelled as a non-resonant coupling loss factor between the rooms. Craik [7] provides a methodology based on an air-spring, which could be extended to other interlayers such as expanded polystyrene (EPS) or mineral wool with different dynamic stiffness. Secondly, the structural fixings will act to transfer energy resonantly from panel to panel. In this case, the transmission also depends on the velocity level of the heavyweight wall construction [8]. There are a number of methodologies to predict resonant sound transmission due to rigid point or line connections including the methodologies in [7,9,10] or spring mounted point connections [11–13]. The more rigid the structural fixings the greater their influence on measured sound insulation improvement, ΔR. The model relies on accurate characterisation of the springs and accurate input data with respect to the surface coverings. (Also, note that in real constructions, the dynamic stiffness may vary if two insulations of identical thermal efficiency but different dynamic stiffness are used together within the same construction.)

These concepts are extended, tentatively, to include curtain wall systems. The main limitations of the current model are that, in addition to accurately characterising the spring-mass system, the resonant transmission through the cavity was not modelled. Thus, only an airtight model without transmission through the cavity is described, which overestimates sound insulation improvement.

2. Theory

The calculation is based on a four subsystem SEA model; this is sketched in Fig. 2. Subsystems 1 and 4 are the source and receiving room subsystems, subsystem 2 is the weatherproof cladding layer, and subsystem 3 is the heavyweight wall. The power is input to the source room (subsystems 1) and it is assumed that there is no backwards flow of energy.

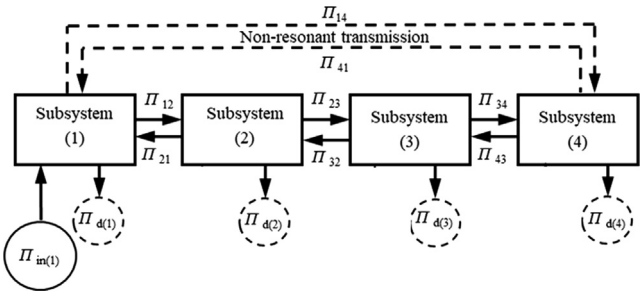

Fig. 2. The four subsystem SEA model (figure formatting Hopkins [11]); subsystem 1 is the source room, subsystem 2 is the weatherproof cladding layer, subsystem 3 is the heavyweight wall, subsystem 4 is the receiving room.

2.1. Expression for ΔR

Previous work has shown that, when the critical frequency of the heavyweight wall is lower than the (first) eigenfrequency of the spring-mass system ($f_{c3} < f_0$), the sound insulation improvement has two principle frequency ranges [14]. A low frequency region where the non-resonant transmission due to the eigenfrequency (or eigenfrequencies) of the spring-mass system dominates and a high frequency region where the resonant transmission through the structural fixings dominates; ΔR across the whole frequency range may be expressed as the summation of these paths. The expression for ΔR in fractional octave bands is shown in Eq. (1). Where wide bands (such as octave or one-third octave) are used f_{cutoff} is set to the centre frequency of the fractional octave band containing the first eigenfrequency of the spring-mass system. For narrower bands f_{cutoff} may be lowered to capture the width of dip at f_0 due to the damping.

$$\Delta R = \begin{cases} 0 & (f < f_{cutoff}) \\ -10log\left(\frac{\eta_{12}\eta_{23}}{\eta_2\eta_{13}} + \frac{\eta_3\eta_{14}}{\eta_{13}\eta_{34}}\right) & (f \geq f_{cutoff}) \end{cases} \quad (1)$$

where η_{12}, η_{13} and η_{34} are radiation coupling loss factors, η_{23} is a resonant coupling loss factor due to the structural connections and η_{14} is a non-resonant coupling loss factor due to the spring-mass system. All components are described in more detail in Section 3.

The following simplifying assumptions are made in the derivation of this expression. The total loss factors of the four subsystem model (Fig. 2) have been assumed to be equal to the equivalent total loss factors in a three subsystem model of the heavyweight wall which is used to obtain the expression for ΔR.

$$\frac{\eta_{3,three\ subsystems}}{\eta_{3,four\ subsystems}} = \frac{\eta_{33}+\eta_{31}+\eta_{34}}{\eta_{33}+\eta_{32}+\eta_{34}} \approx 1 \quad (2)$$

$$\frac{\eta_{4,three\ subsystems}}{\eta_{4,four\ subsystems}} = \frac{T_{4,four\ subsystems}}{T_{4,three\ subsystems}} \approx 1 \quad (3)$$

In the first case (Eq. (2)) the largest quantity in this expression is the internal loss factor η_{33} (which in this case also includes coupling losses at the plate edges). When the gases are identical in the source and receiver rooms $\eta_{32} = \eta_{34}$. In addition, η_{32} is a structural coupling factor and η_{31} is a radiation coupling factor. It can be shown that $\eta_{32} \gg \eta_{31}$, however, the degree of the inequality also depends on the strength of the structural connection between the heavyweight wall and the weatherproof layer e.g. the higher the number of structural connections the greater the inequality. In the second case (Eq. (3)), the total loss factor is a measured

quantity, based on the measured reverberation time of the receiving room. It is assumed that the reverberation time in the receiving room does not change with the addition of the thermal cladding. Overall, these assumptions likely total no more than ±1 dB compared with the full calculation.

2.2. Coupling loss factors

The radiation coupling loss factors are:

$$\eta_{12} = \eta_{21}\frac{n_2}{n_1} = \frac{\rho_1 c_1 \sigma_2}{\omega \rho_{s,2}}\frac{n_2}{n_1} \tag{4}$$

$$\eta_{13} = \eta_{31}\frac{n_3}{n_1} = \frac{\rho_1 c_1 \sigma_3}{\omega \rho_{s,3}}\frac{n_3}{n_1} \tag{5}$$

$$\eta_{34} = \frac{\rho_4 c_4 \sigma_3}{\omega \rho_{s,3}} \tag{6}$$

where ω is the angular frequency, n_1, n_2 and n_3 are the modal densities of the subsystems, ρ_1 and ρ_4 are the densities of the gases in the source and receiving rooms, c_1 and c_4 are the speed of sound in the source and receiving rooms, σ_2 and σ_3 are the radiation efficiencies of the panels, $\rho_{s,2}$ and $\rho_{s,3}$ are the surface densities of the panels. The resonant coupling loss factor due to the structural connections is:

$$\eta_{23} = \frac{r_S}{\omega \rho_{s,2}}\frac{Re\{Y_3\}}{|Y_2 + Y_3 + Y_c|^2} \tag{7}$$

where r_s is the number of structural connections per metre squared, Y_2 and Y_3 are the driving mobilities of the panels and Y_c is the mobility of the structural connections. If the input force is approximated by $2p_1$ [7] the non-resonant coupling loss factor due to the spring-mass system is:

$$\eta_{14} = \frac{c_1 S_2 \rho_4^2 c_4^2}{\omega V_1}|Y_{tr}|^2 \tag{8}$$

Where S_2 is the area of the partition, V_1 is the volume of the receiving room, and Y_{tr}, is the transfer mobility between subsystem 2 and subsystem 3 due to the spring-mass system.

2.3. Total loss factors

Simplifying assumptions were made with respect to the total loss factors in the derivation of eqn. (1) (see Section 2.1). The remaining total loss factors are expressed as follows:

$$\eta_2 = \eta_{22} + \eta_{21} + \eta_{23} \tag{9}$$

$$\eta_3 = \eta_{33} + \eta_{32} + \eta_{34} \tag{10}$$

Where η_{22} and η_{33} are the internal loss factors of the plates and

$$\eta_{32} = \eta_{23}\frac{n_2}{n_3} \tag{11}$$

2.4. Internal loss factors

The internal loss factor of the heavyweight plate takes into account the coupling losses at the edges according to [11]:

$$\eta_{ii} = \eta_{i,internal} + \frac{X}{\sqrt{f}} \tag{12}$$

where X is an empirical factor (in this case chosen to be $X = 0.8$ for the concrete heavyweight walls and $X = 0.3$ for the brick walls) and f is the frequency band of interest. The internal loss factor of the thermal cladding layer was selected according to an appropriate material constant taken from the literature [11]. Coupling at the edges, in this case, was assumed to be minimal and no correction was made.

2.5. Modal densities

The modal densities are given by [11]:

$$n_1 = \frac{4\pi f^2 V_1}{{c_1}^3} + \frac{\pi f S_{T,1}}{2{c_1}^2} + \frac{L_{T,1}}{8c_1} \tag{13}$$

$$n_2 = \frac{S_2\sqrt{3}}{h_2 c_{L,p,2}} \tag{14}$$

$$n_3 = \frac{S_3\sqrt{3}}{h_3 c_{L,p,3}} \tag{15}$$

where $S_{T,1} = 2(L_xL_y + L_xL_z + L_yL_z)$ is the surface area of the source room and $L_{T,1} = 4(L_x + L_y + L_z)$ is the total length of the edges of the source room h_2 and h_3 are the thicknesses of the panels and $c_{L,p,2}$ and $c_{L,p,3}$ are the longitudinal phase velocities of the panels.

2.6. Simplified expression for ΔR (where the gases in the source and receiver room are identical)

A simplified expression for sound insulation improvement (when $f_{c3} < f_0$), ΔR can be rewritten as:

$$\Delta R = \begin{cases} 0 & (f < f_{cutoff}) \\ -10log\left(\frac{n_2}{n_3}\frac{\eta_{21}\eta_{23}}{\eta_2\eta_{31}} + \frac{n_1}{n_3}\frac{\eta_3\eta_{14}}{\eta_{31}\eta_{34}}\right) & (f \geq f_{cutoff}) \end{cases} \tag{16}$$

This results in the simplified expression (when the gases in the source and receiver room are identical):

$$\Delta R = \begin{cases} 0 & (f < f_{cutoff}) \\ -10log\left(\frac{n_2}{n_3}\frac{\sigma_2\rho_{s,3}}{\sigma_3\eta_2\rho_{s,2}^2}\frac{r_S}{\omega}\frac{Re\{Y_3\}}{|Y_2+Y_3+Y_c|^2} + \frac{n_1}{n_3}\frac{\omega\rho_{s,3}^2\eta_3}{\sigma_3^2}\frac{c_0 S_2}{V_1}|Y_{tr}|^2\right) & (f \geq f_{cutoff}) \end{cases} \tag{17}$$

The transfer mobility between subsystem 2 and subsystem 3 according to the spring-mass system and the mobility of the structural connections are examined in more detail below. With respect to the components of the total loss factors, if the radiation losses are assumed to be small ($\eta_{radiation} \ll \eta_{ii}$) they may be ignored and the calculation is further simplified. The condition holds for all frequencies, for the heavyweight wall and, of the models examined, for $f > 100$ Hz for the weatherproof covering. The coupling loss factor, η_{32}, between the heavyweight wall and the weatherproof layer, however, is large and should preferably be included. In the opposite direction the coupling losses are small and may be ignored $\eta_{23} \ll \eta_{22}$. This is true, of the models examined, for $f > 160$ Hz. The expression used to make all calculations was therefore:

$$\Delta R = \begin{cases} 0 & (f < f_{cutoff}) \\ -10log\left(\frac{n_2}{n_3}\frac{\sigma_2\rho_{s,3}}{\sigma_3\eta_{22}\rho_{s,2}^2}\frac{r_S}{\omega}\frac{Re\{Y_3\}}{|Y_2+Y_3+Y_c|^2} + \frac{n_1}{n_3}\frac{\omega\rho_{s,3}^2(\eta_{33}+\eta_{32})}{\sigma_3^2}\frac{c_0 S_2}{V_1}|Y_{tr}|^2\right) & (f \geq f_{cutoff}) \end{cases} \tag{18}$$

2.7. Defining the transfer mobility Y_{tr} and the connection mobility Y_c

2.7.1. Simple spring systems

In the case of simple spring systems, the transfer mobility is [11]:

$$Y_{tr} = \frac{is'}{\omega\left(\omega^2\rho_{s,3}\rho_{s,2} - s'(\rho_{s,3} + \rho_{s,2})\right)} \tag{19}$$

The coupling loss factor between the rooms (subsystems 1 & 4) can therefore be expressed as (including a factor of two account for pressure amplitude addition of the incoming and outgoing waves [7]):

$$\eta_{14} = \frac{c_1 S_2 \rho_4^2 c_4^2}{\omega V_1} \left| \left(\frac{is'}{\omega(\omega^2 \rho_{s,2}\rho_{s,3} - s'(\rho_{s,3} + \rho_{s,2}))} \right)^2 \right| \quad (20)$$

When the gases in the source and receiver room are identical.

$$\eta_{14} = \frac{S_2 \rho_0^2 c_0^3}{\omega V_1} \left| \left(\frac{is'}{\omega(\omega^2 \rho_{s,2}\rho_{s,3} - s'(\rho_{s,3} + \rho_{s,2}))} \right)^2 \right| \quad (21)$$

Which is equivalent to the expression in Craik [7]. In this case the dynamic stiffness ś in Eq. (21) is given by summing the dynamic stiffness of the material interlayer $s'_{\text{interlayer}}$ and the total spring stiffness contribution per unit area for the structural connections.

$$s' = s'_{interlayer} + r_S K \quad (22)$$

Structural damping is introduced using complex spring stiffness $s'(1 + \eta)$ and $K(1 + \eta)$. The possibility to introduce a more complicated combined stiffness is discussed in Section 2.6.2. The mobility of the structural connection in the case of a simple spring (in Eq. (18)) is:

$$Y_c = \frac{i\omega}{K} \quad (23)$$

2.7.2. Multiple spring systems

A multiple spring system could be substituted to determine the non-resonant coupling loss factor and the theory remains the same. The transfer mobility would be required to obtain the velocity difference between the walls (and hence the pressure level difference). This method could be used to determine the coupling loss factor from room to room across a partition comprised of multiple connected springs, frameworks or mass layers, as long as the transfer mobility can be measured or modelled. In the case of a multiple spring system, the concept of a simple spring for the mobility of the structural connections would also likely be inadequate and may therefore require appropriate modification. Unfortunately, this methodology was not tested against the measured results because the spring constants of components of thermal insulation systems are not commonly measured. In further work, methods to measure such components should be developed and tested.

3. Input data for the model

The input data for the models was measured where possible. Not all of the input data for the models was easily acquired (or indeed readily measureable). Therefore, the input data for the models was supplemented, where possible, with values found in the literature. As a last alternative, estimated values were used. The basic input data for the model is summarised in Table 1. The effect of varying these and the other materials which make up the wall is investigated in subsequent subsections 3.1 to 3.4.

Table 1
Input data for the model.

Partition size	2.6 m × 4.0 m
Heavyweight wall	0.2 m concrete or 0.32 m hollow brickwork
Structural connections	Up to 12 springs/m^2 (K = 2.0MNm^{-1})

3.1. Damping of the elastic interlayer

The actual damping for the model was unknown. The damping of the elastic interlayer and structural connections can be separately controlled in the model. It was assumed that the damping of the interlayer was likely greater than the damping of the structural connections, and no damping was included for the structural connections when making a comparison with measured data (see Section 5.1.5). The damping was introduced for the interlayer using a complex spring stiffness $s'(1 + \eta)$ as follows:

$$s' = s'_{interlayer}(1 + i\eta_{s'}) + r_S K \quad (24)$$

Therefore, the estimated total damping for the spring can be calculated as the sum of the spring stiffness according to Eq. (25).

$$s' = (s'_{interlayer} + r_S K)(1 + i\eta_{total}) \quad (25)$$

The estimated total damping is shown in Table 2. To provide more accurate input data in the future the damping could be measured in combination with the dynamic stiffness or when evaluating the spring stiffness of the structural connections.

3.2. Combined dynamic stiffness of the elastic interlayer (or air-spring) and structural connections

The dynamic stiffness of the interlayer was taken from the product information and was measured (according to ISO 9052 [15]). The spring stiffness of the structural connections was set at K = 2.0MNm^{-1}. The combined dynamic stiffness data for the structural connections and the elastic interlayer is shown in Table 3.

3.3. Longitudinal wavespeed and thickness of the weatherproof layer

The longitudinal wavespeed of the render was measured using a time-of-flight pulse method. This methodology has been successfully tested on a number of materials (concrete/lumber/plaster board) [16]. The longitudinal wavespeed was found to be 2230 ms^{-1} and the density assumed to be 1500 kgm^{-3}. The longitudinal wavespeed of the finishing render was varied in 0.005 m increments, (from 0.01 to 0.025 m) to show the effect of increasing the render thickness on the calculated ΔR. A list of alternative materials considered as a weatherproof finishing layer are shown in Table 4.

The limitation to these calculations for other materials is the assumption of flat, airtight systems. In the actual system, however, there may be a cavity between the heavyweight and weatherproof layer, through which power flow could be an important pathway, which is not taken into account in this model. Ornamental features of the façade, such as corrugations, hollows [4], textures and tiling patterns, or architectural features such as curves may alter the bending stiffness. The installation may not be airtight at panel edges or the panels may include decorative perforations. These fac-

Table 2
Estimated total damping in Fig. 1. The spring stiffness for the interlayer and structural connections remains unchanged in the model $s'_{\text{interlayer}}$ = 7.0 MNm^{-3}, r_s = 10, K = 2.0 MNm^{-1} (therefore $s'_{\text{interlayer}} + r_S{\cdot}K$ = 27.0 MNm^{-3}) and the damping of the structural connections η_K = 0.0.

$\eta_{s'}$ (−)	η_{total} (−)
0.1	0.0259
0.2	0.0519
0.4	0.1037
0.6	0.1556

Table 3
Combined dynamic stiffness data and resulting spring-mass resonance f_0, in Fig. 3 and Fig. 4. The spring stiffness for the structural connections remains unchanged in the model r_s = 10, K = 2.0MNm^{-1} and the combined total damping η_{total} = 0.1.

s' (MNm^{-3})	$s'_{interlayer} + r_S \cdot K$ (MNm^{-3})	f_0 (Hz)
4.0	24.0	205
19.0	39.0	261
55.0	75.0	362
115.0	135.0	486

tors may be included in the calculation in a number of ways. The longitudinal wavespeed of the material may be adapted according to the moment of inertia of the cross-sectional-area calculation to approximate the revised bending stiffness [11] (e.g. due to corrugations or other features).

$$c_{i,x} \approx \sqrt{\frac{I_x}{I}} c_i \tag{26}$$

Where I is the moment of inertia of cross-sectional-area of the flat plate and I_x (or I_y) is the moment of inertia of cross-sectional-area e.g. for a corrugated plate I_x (or I_y) is (for $\lambda_B \gg d_R$) [11]:

$$I_x = \frac{h d_z^2}{2}\left[1 - \frac{0.81}{1 + 2.5\left(\frac{d_z}{2d_R}\right)^2}\right] \tag{27}$$

$$I_y = \frac{h^3}{12(1-\nu^2)} \frac{1}{1 + \left(\frac{\pi d_z}{2d_R}\right)^2} \tag{28}$$

Other profiled plates (e.g. sinusoidal corrugations [19]) or forms [11,16,20,21] are also possible. For a plate comprised of I-sections I_x (or I_y) is (for $\lambda_B \gg d_R$) [16,20,21]:

$$I_x = \frac{d_R d_z^3 - d_R(d_z - 2h)^3 + h(d_z - 2h)^3(1-\nu^2)}{12 d_R(1-\nu^2)} \tag{29}$$

$$I_y = \frac{d_R}{12}\left[\frac{d_z^3 h\left(6{d_z}^2 - 12 h d_z + 8h^2\right)}{(d_R - h)d_z^3 + h^2\left(6{d_z}^2 - 12 h d_z + 8h^2\right)}\right] \tag{30}$$

All dimensions are shown in Fig. 3.

In the case of different bending stiffnesses in the x- and y-directions, weak orthotropy is assumed, and an isotropic longitudinal wavespeed can be used as an approximation according to:

$$c_{i,eff} = \sqrt{c_{i,x} c_{i,y}} \tag{31}$$

The plate surface density is adjusted by a factor, $M = A_{eff}/A$, using an effective area according to the extra mass (assuming identical plate thickness).

$$\rho_{s,i,eff} = M \rho_{s,i} \tag{32}$$

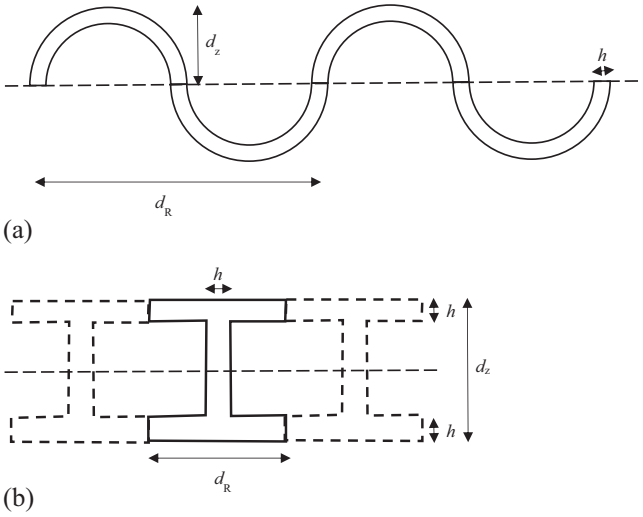

Fig. 3. Dimensions of the cross-sections (a) A corrugated plate [11] (e.g. d_R = 185-mm, d_z = 36 mm, h = 6 mm) (b) A plate comprised of I-sections (e.g. d_R = 40 mm, d_z = 48 mm, h = 8 mm).

For a corrugated plate M is approximated by

$$M \approx \frac{2\pi}{d_R}\left[\frac{1}{2}\left(\left(\frac{d_R}{2}\right)^2 + d_z^2\right)\right]^{1/2} \tag{33}$$

For a plate comprised of I-beams this is calculated according to

$$M = 2 + \frac{(d_z - 2h)}{d_R} \tag{34}$$

Air-gaps, such as between tiles and panels could also be included as a non-resonant coupling loss factor, if the cavity is included in the model as a separate subsystem. However, the consideration of air-gaps is beyond the scope of this paper and not modelled.

3.4. Properties of the heavyweight wall construction

Concrete and solid blockwork of varying thickness (0.15 m, 0.20 m, 0.32 m) and material were investigated. The range of materials considered are listed in Table 5. The limitations of the model are that all plates are assumed to be thin and hollow blockwork is not included.

4. Measurements

Sixteen thermal insulation systems were measured in the laboratory and a comparison was made with calculated results. All systems were measured in an accredited Austrian laboratory. The measurement data is summarised in Table 6.

Table 4
Alternative weatherproof finishing materials in Fig. 7 [17,18].

Material	h (m)	c_i (ms^{-1})	ρ (kgm^{-3})	η_{ii} (−)
Render	0.010–0.025	2230	1500	0.005
Aluminium	0.0007	5100	3430	0.001
Extruded aluminium alloy	0.002	5100	3750	0.001
Aluminium composite	0.004–0.008	5100	1875	0.001
Fibre cement composites	0.0038–0.012	3125	1600–1800	0.005
OSB	0.024	2570	590	0.01
Birch	0.024	3850	710	0.016
MDF	0.024	2560	760	0.01
Clay & ceramics	0.030–0.035	2300	800	0.007

Table 5
Properties of different heavyweight wall constructions [11].

Material	c_i (ms^{-1})	ρ_i (kgm^{-3})	η_{ii} (−)
Solid clinker blocks	1850	1030	0.01
Solid aerated concrete blocks	2300	400	0.0125
Concrete cast in situ	3800	2555	0.005

5. Results

5.1. Damping of the elastic interlayer

The results for different damping constants are shown in Fig. 4. Reasonable estimates for the damping were estimated to be $\eta_{s'}$ = 0.4 and η_K = 0.0.

5.2. Combined dynamic stiffness of the elastic interlayer (or air-spring) and structural connections

The effect of changing the dynamic stiffness of the interlayer according to the values in Table 3 is shown in Fig. 5. Although the stiffness of the point connectors remains the same, as expected, increasing the dynamic stiffness increases the spring-mass resonance frequency of the system. The output data for the combined dynamic stiffness of the interlayer and structural connections can be normalised in two ways: (1) to the critical frequency of the weatherproof layer (in the usual manner by quoting the 1/24th octave bands, see Fig. 5(a)), or (2) to the spring-mass resonance (by quoting normalised 1/24th octave bands f/f_0), see Fig. 5(b)). This latter form may be useful for visualising the impact on high frequencies without the corresponding shift in f_0. However, it is only useful when the critical frequency of the weatherproof layer is much higher than the spring–mass resonance of the weatherproof layer ($f_{c2} \gg f_0$) and preferably out of the frequency range of interest ($f_{c2} \gg$ 5000 Hz).

In the simplified calculation model, the resonant coupling loss factor (η_{23}) depends only on the dynamic stiffness of the structural connections, not on the dynamic stiffness of the elastic interlayer. The model, therefore, will fail in the case of zero connections. This was not thought to be a major drawback; as thermal cladding systems are rarely, if ever, installed without structural fixings. The number of structural connections and their dynamic stiffness are examined in Fig. 6. When the critical frequency of the weatherproof layer is not an order of magnitude higher than the spring-mass resonance frequency ($f_{c2} \gg f_0$), the benefit of decreasing the number of structural connectors (or their spring stiffness) over the whole frequency range is clearly reduced (dotted lines with and without markers).

5.3. Thickness and longitudinal wavespeed of the weatherproof layer

5.3.1. Render

Different thicknesses of finishing render are considered in Fig. 7 (a). The effect of the shifting spring-mass resonance combined with the shifting critical frequency can be clearly seen. (Note that the model is more successful for thick renders ($\geq$ 0.008 m) than thin, see Section 5.1.5). In the results for thicker renders ($h_2 \geq$ 0.015 m), the curves are truncated at low frequencies as f_0 approaches f_{c3} ($h_2 \geq$ 0.008 m).

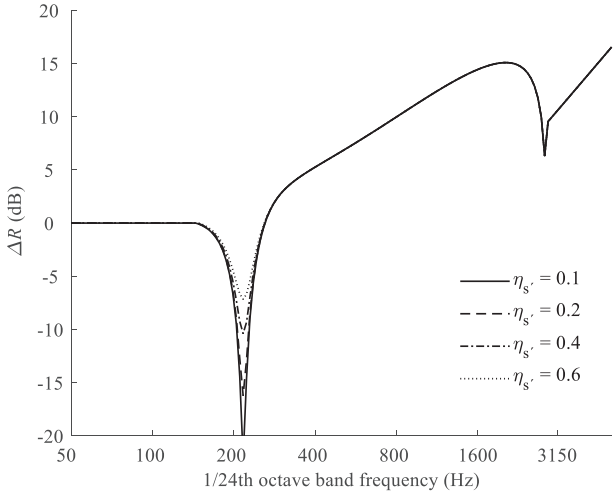

Fig. 4. The effect of damping of the interlayer. (In all models c_0 = 343 ms^{-1}, ρ_0 = 1.205 kgm^{-3}, c_2 = 2230 ms^{-1}, ρ_2 = 1500kgm^{-3}, h_2 = 0.01 m, η_2 = 0.005, c_3 = 3000 ms^{-1}, ρ_3 = 1500 kgm^{-3}, h_3 = 0.2 m, η_3 = 0.005, $s'_{\text{interlayer}}$ = 7.0 MNm^{-3}, r_s = 10, K = 2.0 MNm^{-1}, η_K = 0.0 and the radiation efficiencies are capped at and above the critical frequencies at σ_2 = 1.0, σ_3 = 1.0.)

5.3.2. Other material finishes

The ΔR for different material finishes is shown in Fig. 7(b), (c) and (d). The sound insulation improvement varies greatly according to the weatherproof finish. Truncation effects are also visible for many of the materials: thick fibre cement composites, clay and ceramics, aluminium, thick aluminium composites and wood products, which may affect the overall accuracy of the predicted result.

The effect of the changing cross-section of the flat (ceramic) plate to a corrugated plate or plate comprised of I-sections of the same material is shown in Table 7. The ratio $c_{L,x}/c_{L,y}$ is calculated to show the degree of orthotropy of the plate. The corrugated plate is considerably orthotropic and the assumption of weak orthotropy may not hold in this case. If weak orthotropy cannot be assumed, then it may be more appropriate to incorporate an orthotropic model (such as [22]) into the SEA framework. The ratio $c_{L,\text{eff}}/c_L$ is calculated to show the change in bending stiffness of the plate, and the I-section plate is much stiffer in bending than the corrugated plate. Note, however, that the I-section plate may no longer behave as a thin plate.

The sound insulation improvement of these different plate profiles (in Table 7) are compared in Fig. 8. Wider fractional octave bands are presented, and a larger frequency range (up to 32000 Hz) to emphasise the frequency ranges of applicability of

Table 6
List of measured data.

Heavyweight wall	Spring system	Weatherproof Layer
0.2 m Concrete	EPS and 6/10/12 fixings/m^2	5 mm render
0.2 m Concrete	EPS and 12 fixings/m^2	10 mm render
0.2 m Concrete	Mineral wool and 6 fixings/m^2	5 mm/10 mm render
0.32 m Brick	EPS and 6/10/12 fixings/m^2	5 mm/10 mm render
0.32 m Brick	Mineral wool and 10 fixings/m^2	4 mm/8mm render
0.2 m Concrete	Curtain wall system 1.73 fixings/m^2 (0.20 m airgap)	4 mm Aluminium composite
0.2 m Concrete	Curtain wall system 1.73 fixings/m^2 (0.24 m airgap)	8 mm Fibre cement composite

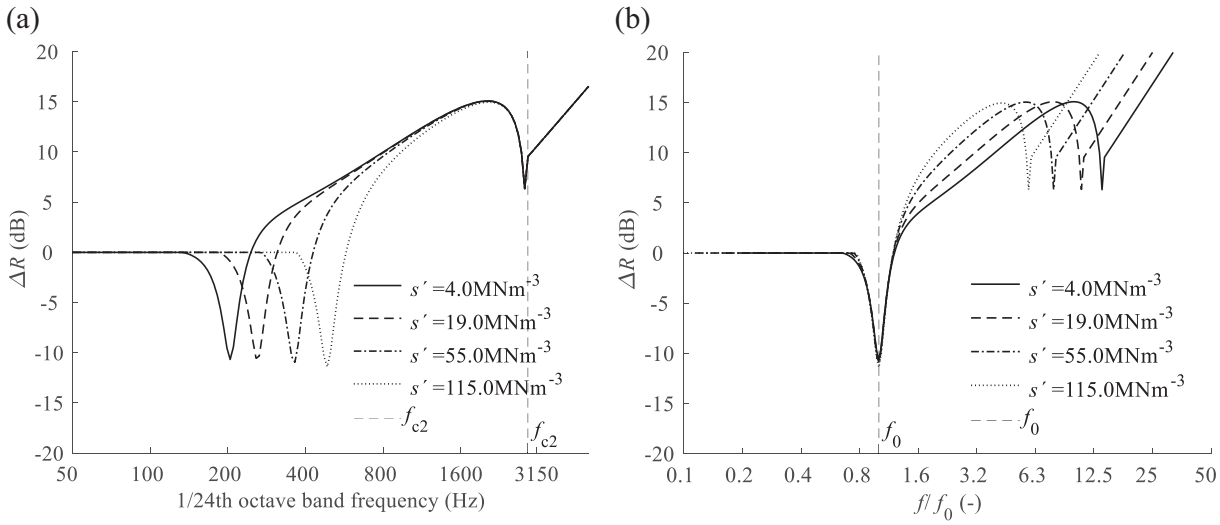

Fig. 5. The effect of dynamic stiffness of the interlayer. (a) 1/24th octave bands (b) Normalised 1/24th octave bands f/f_0 (In all models c_0 = 343 ms^{-1}, ρ_0 = 1.205 kgm^{-3}, c_2 = 2230 ms^{-1}, ρ_2 = 1500 kgm^{-3}, h_2 = 0.01 m, η_2 = 0.005, c_3 = 3000 ms^{-1}, ρ_3 = 1500 kgm^{-3}, h_3 = 0.2 m, η_3 = 0.005, r_s = 10, K = 2.0MNm^{-1}, η_K = 0.1, $\eta_{s'}$ = 0.1 and the radiation efficiencies are capped at and above the critical frequencies at σ_2 = 1.0, σ_3 = 1.0.)

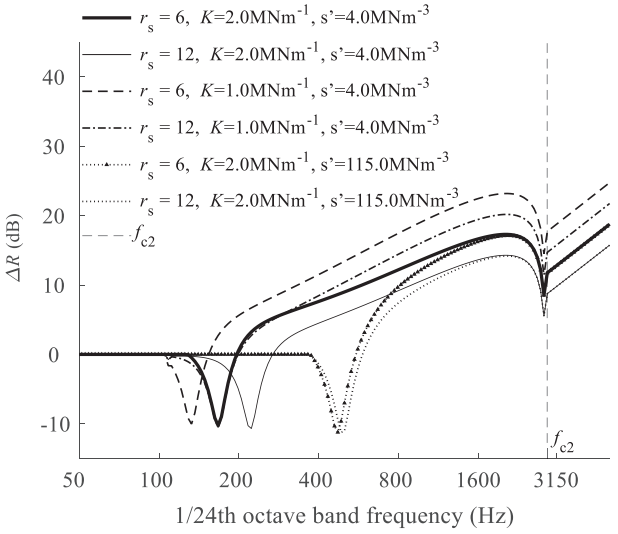

Fig. 6. The effect of altering the stiffness and number of the structural connectors with a low dynamic stiffness interlayer compared with a high dynamic stiffness interlayer. (In all models c_0 = 343 ms^{-1}, ρ_0 = 1.205 kgm^{-3}, c_2 = 2230 ms^{-1}, ρ_2 = 1500 kgm^{-3}, h_2 = 0.01 m, η_2 = 0.005, c_3 = 3000 ms^{-1}, ρ_3 = 1500 kgm^{-3}, h_3 = 0.2 m, η_3 = 0.005, s' = 4.0 MNm^{-3} or 115.0 MNm^{-3}, K = 1.0 MNm^{-1} or 2.0 MNm^{-1}, η_K = 0.1, $\eta_{s'}$ = 0.1 and the radiation efficiencies are capped at and above the critical frequencies at σ_2 = 1.0, σ_3 = 1.0.)

the examples. Note that $\lambda_B \gg d_R$ is quoted [11], however, the appropriate ranges of applicability (and transition zones) should be confirmed by measurement. The modal density of alternative plate profiles may be lower than that of the thin homogenous plate therefore the frequency averaged radiation efficiency may not be an adequate estimate of the radiation efficiency at and below the critical frequency. In which case, calculation of the radiation of individual modes may be more appropriate [11].

Verification of the fundamental eigenfrequencies of the plates would require knowledge of their size; in the case of tiles, the size could be very small. (If the plate comprised of I-sections is assumed to consist of one simply supported panel, 4.0 m × 2.6 m, the modes of the panel are $f_{1,1}$ = 39.8 Hz, $f_{2,1}$ = 75.3 Hz, $f_{1,2}$ = 123.8 Hz, $f_{3,1}$ = 134.4 Hz, $f_{2,2}$ = 159.3 Hz.) The critical frequency of the plate is lowered for the corrugated plate, and further lowered for the plate comprised of I-sections. For the I-section plate profile (where f_{c2} = 155 Hz) the critical frequency is below the spring-mass resonance ($f_{c2} < f_0$) and the applicability of Eq. (18) to predict the sound insulation improvement, should this occur within the frequency range of interest, is unclear.

5.4. Properties of the heavyweight wall construction

The effect of changing the heavyweight wall construction is non-zero but largely negligible in the calculation. The effect of changing the internal loss factor of the heavyweight wall is negligible especially when the factor describing coupling losses at the edges is large ($X \geq 0.3$ in the cases shown). The main aspects are summarised by changing the longitudinal wavespeed and surface density within reasonable bounds as shown in Fig. 9(a) and (b). The crucial requirement for the heavyweight wall is that its critical frequency is lower than the (first) eigenfrequency of the spring-mass system ($f_{c3} < f_0$).

5.5. Comparison with measured data

The comparison between modelled and measured data for the systems is shown in Figs. 10–14. The most striking observation from these results is that the measured high frequency ($f > f_0$) sound insulation improvement (see Figs. 10 and 11) is much more dependent on the properties of the heavyweight wall than the modelled results (see Section 5.1.4). This effect is even more pronounced for the mineral wool rather than the EPS thermal interlayer. The spring-mass resonance(s) of the systems are dependent not only on the stiffness of the elastic interlayer but also on the spring stiffness of the structural connections. The spring stiffness of the structural connection was unknown and therefore estimated. An identical estimated stiffness is used in calculations for both the EPS and mineral wool, despite longer connectors in the latter case potentially reducing the connector stiffness. This could account for the apparently lower f_0 in the measured data.

The overall effectiveness of the model was assessed in three groups: for thin render ($h_2 \leq 5.0$ mm), thick render ($h_2 \geq 8.0$ mm), and for the curtain wall systems. The mean absolute dif-

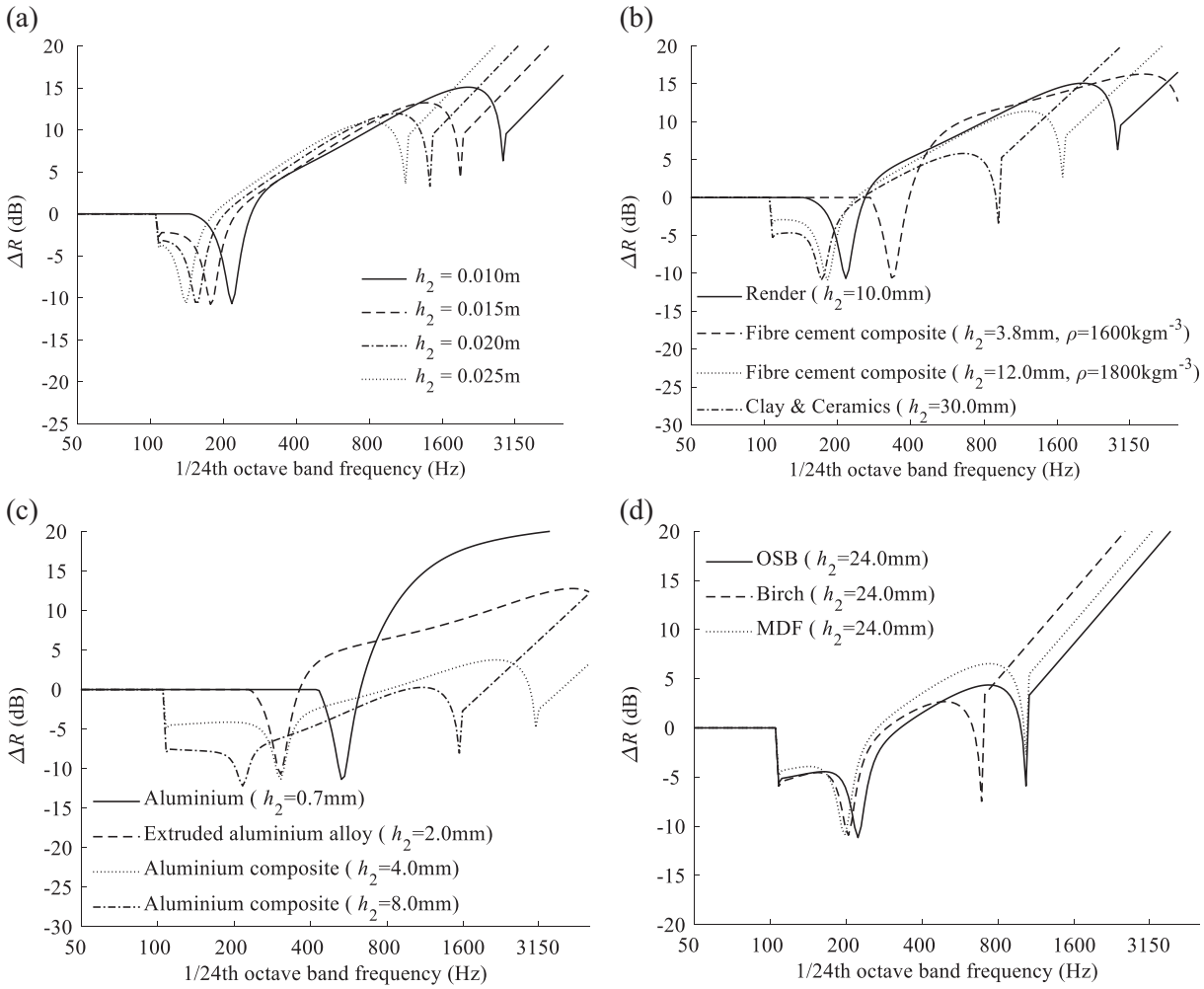

Fig. 7. Comparison of different material finishes: (a) Render of different thicknesses. (b) Render, fibre cement composite, clay and ceramics. (c) Aluminium, alloys and composites. (d) Wood products. (In all models c_0 = 343 ms^{-1}, ρ_0 = 1.205 kgm^{-3}, η_2 = 0.005, c_3 = 3000 ms^{-1}, ρ_3 = 1500 kgm^{-3}, h_3 = 0.2 m, η_3 = 0.005, s′ = 7.0MNm^{-3}, r_s = 10, K = 2.0 MNm^{-1}, η_K = 0.1, $\eta_{s'}$ = 0.1 and the radiation efficiencies are capped at and above the critical frequencies at σ_2 = 1.0, σ_3 = 1.0.)

Table 7
Effective longitudinal wavespeed ($c_{L,eff}$) and effective surface density ($\rho_{s\ ,eff}$) (assuming identical plate thickness) for two examples.

	h (mm)	d_R (mm)	d_z (mm)	ρ_s or $\rho_{s\ ,eff}$ (kgm^{-2})	c_L or $c_{L,eff}$ (ms^{-1})	$c_{L,x}/c_{L,y}$ (−)	$c_{L,eff}/c_L$ (−)
Flat plate	6	–	–	4.8	2300	1.0	–
Corrugated plate	6	185	36	5.7	5485	7.6	2.4
I-section plate	6	40	48	13.9	41,736	1.0	18.1

ferences for each group are shown in Table 8. At low frequencies ($f \leq f_0$), the thin and thick renders deviate strongly from the assumption that ΔR = 0, suggesting that an improved evaluation of Y_{tr} may be necessary to accurately capture the low frequency behaviour. It is difficult to say whether this low frequency behaviour is due to the spring system or low modal density in the subsystems. Low modal density in the subsystems may also be the cause of inaccuracy for the curtain wall systems.

Despite the aforementioned limitations of the model, the mean absolute differences in Table 8 suggest consistently closer calculated results to the measured results for thick render compared with thin render. The closest agreement at high frequencies (f > 1250 Hz) is obtained for the thick render systems (mean absolute differences < 6.0 dB). The main limitation for thick renders being a lack of definitive critical frequency dip in the measured data. In the mid frequency range (315–1250 Hz), the closest agreement between measured and modelled results are obtained for the thick render and curtain walls (with mean absolute differences < 4.0 dB). The structural mounting system was altered in the curtain wall systems. Therefore, the number of structural connections and estimated spring stiffness was adjusted accordingly. The curtain wall units were also sealed with tape to improve their airtightness. Nevertheless, poor agreement between measured and modelled results at high frequencies (f >1000 Hz) for the curtain walls could still be attributed due to the lack of airtightness of these systems.

Success at modelling the frequency range above f_0 did not equate to success at modelling weighted sound reduction index. A comparison between measured and modelled single figure values (for the

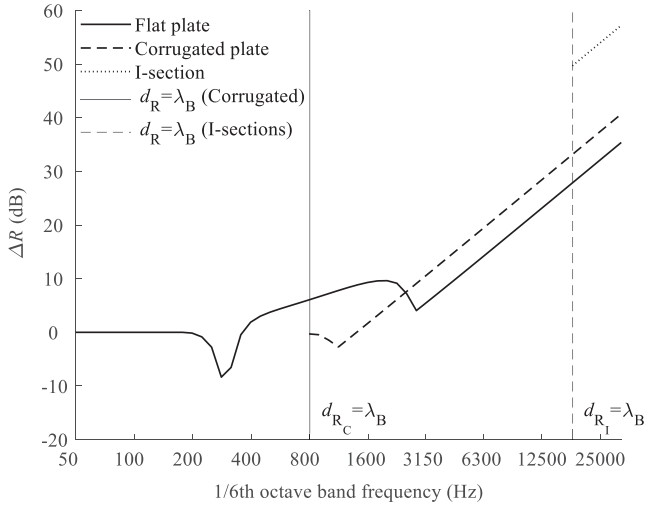

Fig. 8. Comparison between a flat plate, corrugated plate and I-section of identical material properties (see Table 7). (In all models c_0 = 343 ms^{-1}, ρ_0 = 1.205 kgm^{-3}, η_2 = 0.005, c_3 = 3000 ms^{-1}, ρ_3 = 1500 kgm^{-3}, h_3 = 0.2 m, η_3 = 0.005, s'=7.0 MNm^{-3}, r_s = 10, K = 2.0 MNm^{-1}, η_K = 0.1, $\eta_{s'}$ = 0.1 and the radiation efficiencies are capped at and above the critical frequencies at σ_2 = 1.0, σ_3 = 1.0.)

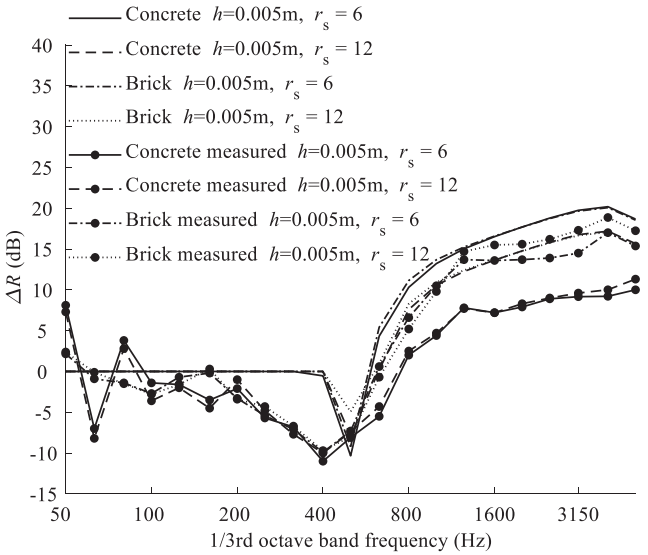

Fig. 10. Comparison between calculated and measured results for thin render, EPS, and different numbers of connector. (In all models the radiation efficiencies are capped at and above the critical frequencies at σ_2 = 1.0, σ_3 = 1.0.)

ETICS listed in Table 6) is shown in Fig. 15; only two systems are accurately predicted. Finally, the relationship between the spring-mass resonance frequency of the sixteen ETICS systems listed in Table 6, and the weighted sound insulation improvement was reassessed. This time the spring-mass resonance frequency was calculated using a combined spring stiffness, Eq. (25). The closeness of the data points to a trendline was slightly improved, although note that the stiffness of the point connectors was based on an estimate (r.m.s. differences of 2.62 compared with 3.21 using the f_0 calculation methodology in EN ISO12354 Annex D). The single figure rating (ΔR_W) is weighted towards the low frequencies ($f \leq f_0$) and therefore highly dependant on accurate modelling within this frequency range. If the low frequencies can be accurately characterised, a revised relationship may yet be possible between the spring-mass resonance frequencies of the spring-mass system, which would result in accurate predictions of the single figure rating.

6. Conclusions

The simplified model is based on an SEA path analysis, which assumes that the sum of paths must be equal to the full matrix solution. This condition was met in all of the simulations described, which supports the proposal to flexibly apply the methodology to different types of systems. The main limitation encountered with the input data described throughout the paper is that the measured high frequency ($f > f_0$) sound insulation improvement is much more dependent on the properties of the heavyweight wall than anticipated.

In the low frequency range ($f \leq f_0$), the concept of a simple spring in thermal insulation systems is limited and may result in an inaccurate prediction of weighted sound insulation improvement. Thermal insulation systems likely involve combined interactions of multiple springs, which influence the sound insulation

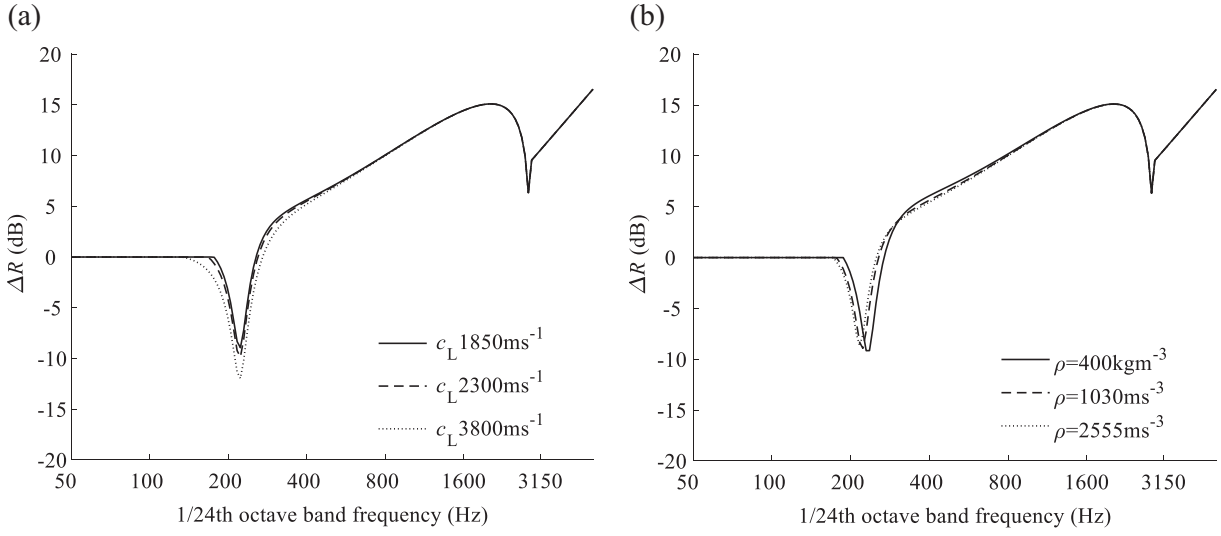

Fig. 9. Comparison between (a) different longitudinal wavespeeds of the heavyweight wall. (b) Different surface densities of the heavyweight wall. (In all models c_0 = 343 ms^{-1}, ρ_0 = 1.205 kgm^{-3}, c_2 = 2230 ms^{-1}, ρ_2 = 1500 kgm^{-3}, h_2 = 0.01 m, η_2 = 0.005, η_3 = 0.005, s' = 7.0 MNm^{-3}, r_s = 10, K = 2.0 MNm^{-1}, η_K = 0.1, $\eta_{s'}$ = 0.1 and the radiation efficiencies are capped at and above the critical frequencies at σ_2 = 1.0, σ_3 = 1.0.)

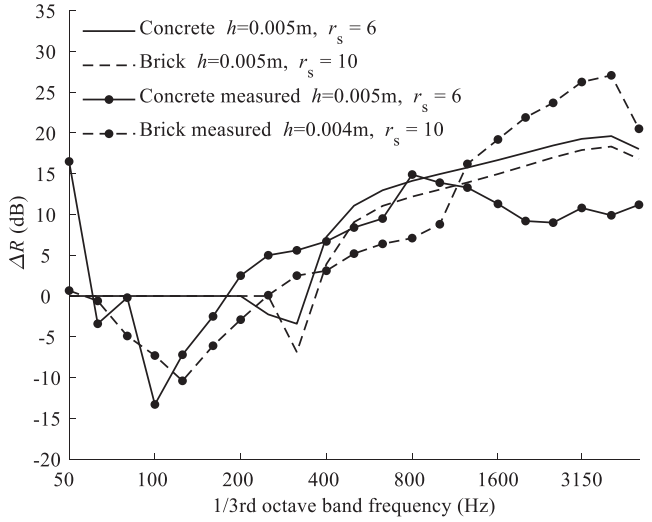

Fig. 11. Comparison between calculated and measured results for thin render mineral wool and different numbers of connector. (In all models the radiation efficiencies are capped at and above the critical frequencies at σ_2 = 1.0, σ_3 = 1.0.)

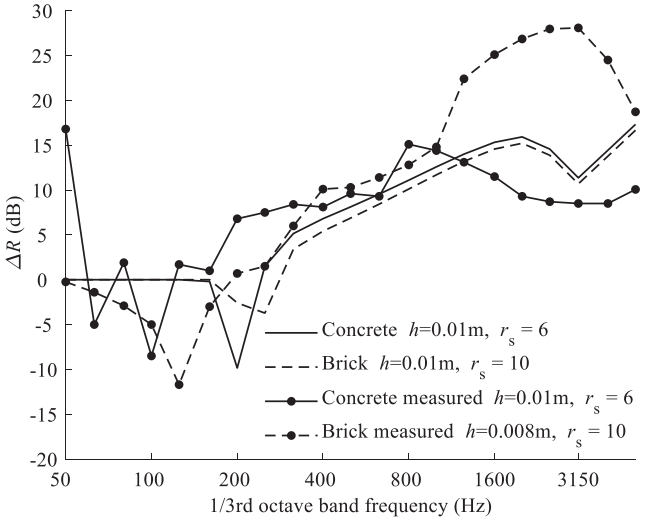

Fig. 13. Comparison between calculated and measured results for thick render, mineral wool and different numbers of connector. (In all models the radiation efficiencies are capped at and above the critical frequencies at σ_2 = 1.0, σ_3 = 1.0.)

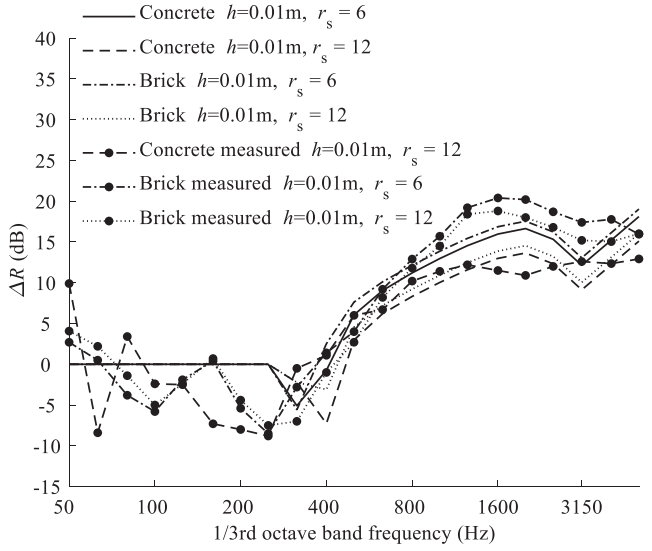

Fig. 12. Comparison between calculated and measured results for thick render, EPS and different numbers of connector. (In all models the radiation efficiencies are capped at and above the critical frequencies at σ_2 = 1.0, σ_3 = 1.0.)

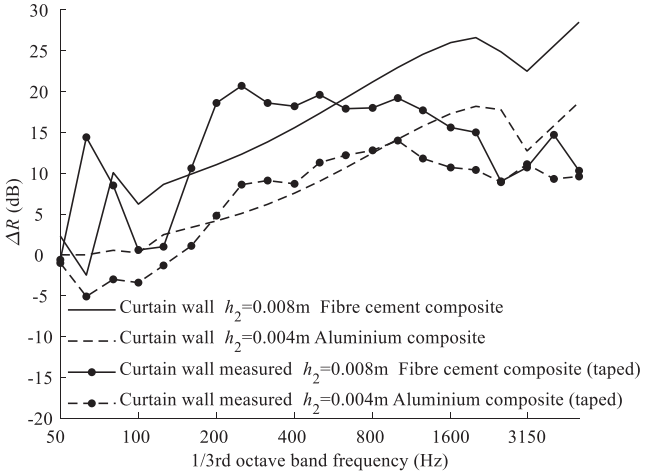

Fig. 14. Comparison between calculated and measured curtain walls. (In all models c_0 = 343 ms^{-1}, ρ_0 = 1.205 kgm^{-3}, c_3 = 3800 ms^{-1}, ρ_3 = 2555 kgm^{-3}, η_3 = 0.005, r_s = 1.76, K = 1.2MNm^{-1}, η_K = 0.1, $\eta_{s'}$ = 0.1, the air-spring is given by $s' = c_0^2\rho_0/\gamma d$ where d is the airgap, γ = 1.41 is the ratio of specific heats and the radiation efficiencies are capped at and above the critical frequencies at σ_2 = 1.0, σ_3 = 1.0.)

improvement at low frequencies. A deeper understanding of the influence of individual springs on the transfer function of the spring-mass system is required, to enable the separation of these sound insulation characteristics from other causes. Additional mechanisms that may cause peaks or troughs in the sound insulation improvement include prominent bending or room modes, which may also shift when the material properties are changed. The methodology by which the stiffness of individual springs and the other component parts interact to form the transfer function

Table 8
Mean absolute differences for thin render (≤5.0 mm), thick render (≥8.0 mm), and for the curtain wall systems.

f (Hz)	50	63	80	100	125	160	200	250	315	400	500
Thin	5.9	3.6	2.7	4.7	3.3	3.0	2.6	4.8	7.5	7.6	5.9
Thick	6.1	3.1	2.9	5.9	3.8	2.2	7.0	7.2	3.2	3.2	6.1
Curtain wall	2.0	11.0	2.6	4.6	5.7	1.5	4.1	6.0	3.8	1.9	2.0
f (Hz)	630	800	1000	1250	1600	2000	2500	3150	4000	5000	
Thin	2.3	4.8	4.5	4.0	3.4	4.8	5.4	5.7	6.1	6.4	
Thick	2.5	1.1	2.4	2.5	4.3	4.8	5.1	4.9	6.4	3.7	
Curtain wall	2.3	1.4	1.8	2.0	5.4	8.5	9.7	12.4	6.7	8.7	

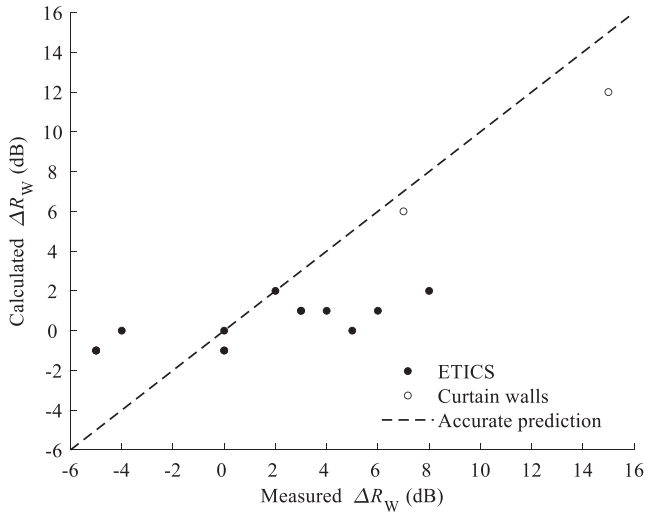

Fig. 15. Comparison between calculated and measured ΔR_W for the different thermal cladding systems listed in Table 6; some data points are concurrent. Data points, falling on the dotted line indicate accurate predictions.

is required to advance the calculation model. The single figure rating is highly dependent on accurate modelling of the low frequencies. This is likely the key to obtaining accurate single figure sound insulation improvement values, because these values are weighted towards the low frequencies. A revised relationship between the spring-mass resonance frequencies of the spring-mass system to obtain accurate predictions of the single figure rating may follow.

Curtain wall systems differ only in that the requirement to know the dynamic stiffness of the thermal interlayer is eliminated by means of an air–gap. The air acts as the spring rather than the insulating material. Such systems are thus highly effective at improving the sound insulation of the heavyweight wall by means of lowering the spring-mass resonance of the system outside of the building acoustics range (f_0 < 100 Hz). However, the airtightness of such systems is also an important consideration.

CRediT authorship contribution statement

C. Churchill: Project administration, Conceptualization, Methodology, Software, Writing - original draft, Writing - review & editing, Visualization. **T. Bednar:** Supervision, Funding acquisition, Data curation, Writing - review & editing. **H. Müllner:** Supervision, Funding acquisition, Data curation, Resources. **M. Neusser:** Project administration, Funding acquisition, Investigation. **S. Hinterseer:** Investigation.

Declaration of Competing Interest

The authors declare that they have no known competing financial interests or personal relationships that could have appeared to influence the work reported in this paper.

Acknowledgments

The work carried out this project was supported jointly by the FFG (Österreichische Forschungsförderungsgesellschaft) (60% funding) [Projektnummer: 864983], and commercial project partners (40% funding). We gratefully acknowledge Michaela Smertnig and Johannes Zeilinger from Ecoplus, Niederösterreich-Ring 2, Haus A, 3100 St. Pölten for project management and guiding communication with the commercial project partners. The authors acknowledge TU Wien Bibliothek for financial support through its Open Access Funding Programme.

References

[1] Magrini A, Scamoni F, Scrosat C. Integrated acoustic and thermohygrometric performances of building walls, for more efficient refurbishment strategies: first evaluations. ICSV21, Beijing, China, 2014.
[2] Guigou-Carter C, Foret R, Villot M, Chéné J-B. "Effect of thermal renovation on acoustic performance of buildings. Euronoise, Edinburgh, Scotland, 2009.
[3] Parati L, Farbood BP, Borghi M. May retrofit also include acoustics aspects? Energy Procedia 2015;78:158–63.
[4] Nurzynski J. The effect of additional thermal lining on the acoustic performance of a wall. Euronoise, Paris, France, 2008.
[5] ISO12354-1 Building acoustics - Estimation of acoustic performance of buildings from the performance of elements Part 1: Airborne sound insulation between rooms, International Organization for Standardization, 2017.
[6] ISO10140-1 Acoustics — Laboratory measurement of sound insulation of building elements, International Organization for Standardization, 2016.
[7] Craik RJM. Sound transmision through buildings using statistical energy analysis. Gower 1996.
[8] Santoni A, Bonfiglio P, Davy JL, Fausti P, Pompoli F, Pagnoncelli L. Sound transmission loss of ETICS cladding systems considering the stucture-borne transmission via the mechanical fixings: Numerical prediction model and experimental evaluation. Appl Acoust 2017;122:88–97.
[9] Vigran TE. Building acoustic. Taylor & Francis; 2008.
[10] Cremer L, Heckl M, Petersson BAT. Structure-borne sound. Germany: Springer; 2005.
[11] Hopkins S. Insulation. Elsevier; 2007.
[12] Craik RJM, Smith RS. Sound transmission through lightweight parallel plates. Part II: structure-borne sound. Appl Acoust 2000;61:247–69.
[13] Craik RJM, Wilson R. Sound transmission through masonry cavity walls. J Sound Vib 1995;179:79–96.
[14] Churchill C, Neusser M, Hinterseer S. Determining the airborne sound insulation improvement of thermal cladding systems in combination with heavyweight exterior walls. Proceeding of the 23rd International Congress on Acoustics, Aachen, 2019.
[15] ISO 9052 Acoustics — Determination of dynamic stiffness, International Organization for Standardization, 1989.
[16] Churchill C. Direct and flanking transmission across timber concrete composite floors with cross laminated timber walls. University of Liverpool; 2018.
[17] Fassaden - Produkte, Eternit, [Online]. Available: https://www.eternit.at/produkte/. [Accessed 20 April 2020].
[18] Produkte - Fassadensysteme, Wienerberger, [Online]. Available: https://www.wienerberger.at/produkte/fassade/produktgruppe.html. [Accessed 2020 April 20].
[19] Ye Z, Berdichevsky VL, Yu W. An equivalent classical plate model of corrugated structures. Int J Solids Struct 2014;51:2073–83.
[20] Huffington NJ. Bending athwart a parallel stiffened plate. J Appl Mech 1976;34 (2):278–82.
[21] Troitsky MS. Stiffened plates: bending stability and vibrations. Elsevier; 1976.
[22] Leppington FG, Heron KH, Broadbent EG. Resonant and non–resonant transmission of random noise through complex plates. Proc R Soc Lond A 2002;458(2019):683–704.